



## Full Length Article

# Hierarchical synthesis of corrugated photocatalytic TiO<sub>2</sub> microsphere architectures on natural pollen surfaces

Deniz Altunoz Erdogan, Emrah Ozensoy <sup>\*</sup>,<sup>1</sup>

Department of Chemistry, Bilkent University, 06800, Ankara, Turkey

## ARTICLE INFO

## Article history:

Received 12 October 2016

Received in revised form 7 January 2017

Accepted 12 January 2017

Available online 17 January 2017

## Keywords:

TiO<sub>2</sub>

Photocatalyst

Ambrosia trifida

NO(g) oxidation

Rhodamine B

## ABSTRACT

Biomaterials are challenging, yet vastly promising templates for engineering unusual inorganic materials with unprecedented surface and structural properties. In the current work, a novel biotemplate-based photocatalytic material was synthesized in the form of corrugated TiO<sub>2</sub> microspheres by utilizing a sol-gel methodology where *Ambrosia trifida* (*Ab*, Giant ragweed) pollen was exploited as the initial biological support surface. Hierarchically synthesized TiO<sub>2</sub> microspheres were structurally characterized in detail via SEM-EDX, Raman spectroscopy, XRD and BET techniques in order to shed light on the surface chemistry, crystal structure, chemical composition and morphology of these novel material architectures. Photocatalytic functionality of the synthesized materials was demonstrated both in gas phase as well as in liquid phase. Along these lines, air and water purification capabilities of the synthesized TiO<sub>2</sub> microspheres were established by performing photocatalytic oxidative NO<sub>x</sub>(g) storage and Rhodamine B(aq) degradation experiments; respectively. The synthetic approach presented herein offers new opportunities to design and create sophisticated functional materials that can be used in micro reactor systems, adsorbents, drug delivery systems, catalytic processes, and sensor technologies.

© 2017 Elsevier B.V. All rights reserved.

## 1. Introduction

Hazardous chemicals arising from combustion of fossil fuels, such as sulphur dioxide, nitrogen oxides, mercury, as well as industrial waste material including organic dyes, and solvents are among the prominent contaminants contributing to the water, air and soil pollution; causing a wide variety of severe health and environmental problems [1–5]. Heterogeneous catalysis plays an important role in coping with the environmental pollution at the global scale. One of the most abundant renewable energy sources that can be exploited in heterogeneous catalysis applications in an environmentally friendly and economical manner is the solar energy. Thus, there exists an immense demand to develop novel photocatalytic materials using innovative synthetic methodologies [6–11].

A large variety of materials such as metal oxides, metal hydroxides, metal carbides, metal nitrides, carbon allotropes and their derivatives have been investigated in the literature as photocatalysts [12–18]. Among them, titanium dioxide (TiO<sub>2</sub>) has received considerable attention since the successful generation of H<sub>2</sub> from water via electrochemical photolysis of water by Fujishima and

Honda [19]. TiO<sub>2</sub> has been the most frequently utilized photocatalytic material due to its functional versatility in a wide range of processes such as energy storage/conversion, photocatalytic pollution abatement, and biotechnology [20–22].

It is well known that physical and chemical properties of materials such as shape, texture, particle size, porosity, specific surface area, crystallinity, electronic band gap, surface defects and surface functional groups directly influence the photocatalytic performance. Particularly, shape and surface structural properties of photocatalytic materials can be closely linked to the reactivity and selectivity of these systems [23–25]. One of the most efficient and simple approaches to prepare sophisticated surface structures on materials is templating. Natural/biological starting materials can be used as temporal support systems/sacrificial templates in order to create well-defined shapes, sizes and textures on surfaces. For instance, mesoporous hollow SnO<sub>2</sub> microfibers were prepared using natural kapok (*Ceiba pentandra*) fiber as a template and were found to be photocatalytically active in methylene blue dye degradation under UV irradiation [26]. In another study, fresh natural rose (*Rosa hybrida* L.) petals were used as a template to synthesize TiO<sub>2</sub> flakes exhibiting higher photocatalytic activity than the commercial Degussa P25 photocatalyst [27]. Also, cerium-doped TiO<sub>2</sub> mesoporous nanofibers were prepared by a single-pot synthesis method using collagen fiber

<sup>\*</sup> Corresponding author.E-mail address: [ozensoy@fen.bilkent.edu.tr](mailto:ozensoy@fen.bilkent.edu.tr) (E. Ozensoy).<sup>1</sup> Web: <http://www.fen.bilkent.edu.tr/~ozensoy>

biotemplates [28]. A variety of synthetic techniques have been developed to deposit the desired photocatalytic material on the surface of bio-templates including sputtering, sol-gel, electrochemical deposition, and chemical vapour deposition approaches. Using such synthetic methods, micro/nanostructures such as wires, tubes, rods or spheres can be fabricated preserving the original shape and size of the initial natural template. Pollen grains attract attention as versatile biotemplates due to their unique and sophisticated surface structures at the micro/nanoscale [7,29–33].

Thus, in the present study, a simple biotemplate assisted sol-gel route is presented in order to synthesize TiO<sub>2</sub> photocatalytic microspheres with unique surface morphologies, where Ambrosia trifida (*Ab*, Giant ragweed) pollen is used as the starting bio-substrate. *Ab* is selected as a biotemplate due to its unusual micron-sized surface morphology exhibiting conical nano-spikes. Upon detailed structural characterization of this novel material platform, photocatalytic functionality of these hierarchical systems under ultraviolet-A (UVA) irradiation is also demonstrated at two different interfaces namely, Rhodamine B (*RhB*) photodegradation at the liquid/solid interface as well as the photocatalytic oxidative storage of NO<sub>x</sub>(g) at the gas/solid interface; illustrating the catalytic versatility of this new family of materials.

## 2. Experimental

### 2.1. Materials

*Ambrosia trifida* (*Ab*, Giant ragweed) pollens were obtained from Bonapol a.s. Company (Czech Republic). Titanium (IV) isopropoxide (TIP, 97%), ethanol ( $\geq 99.8\%$ ), and Rhodamine B (*RhB*, dye content  $\sim 95\%$ ) were purchased from Sigma-Aldrich (Germany). All chemicals were of analytical grade and used as received without any further treatment. Milli-Q ultra-pure deionized water (18.2 MΩ cm) was also used as a solvent.

### 2.2. Synthesis of biotemplated TiO<sub>2</sub> microspheres

Biotemplated TiO<sub>2</sub> microspheres were prepared using a method analogous to the one described in one of our previous reports [7]. Briefly, *Ab* pollens were washed with anhydrous ethanol to remove surface impurities and subsequently dried under ambient conditions for 48 h. Then, titanium (IV) isopropoxide (TIP, 4 mL) precursor was mixed with ethanol (2 mL) for a period of 10 min at room temperature. 100 mg clean *Ab* pollen (*i.e.*, biotemplate) was added to the prepared precursor solution and the slurry was stirred vigorously for 30 min. After depositing precursor solution on the outer surface (*i.e.* exine) of the biotemplate, the mixture was filtered to remove the excess decantate. Coated sample was aged for 60 min under ambient conditions in order to allow for the hydrolysis and polycondensation reactions to proceed, forming an amorphous TiO<sub>2</sub> shell on the biotemplate surface. Then, calcination steps were executed in a muffle furnace at various temperatures varying within 400 °C–900 °C (for 2.5 h per calcination step) in air, where the sacrificial biotemplate was eliminated and the crystallization and ordering of the TiO<sub>2</sub> overlayer were achieved. Products obtained at the end of the synthesis protocol are named as *AbTi-X*, where X indicates the calcination temperature.

### 2.3. Characterization

Surface structure and morphology of the samples were investigated via a Carl-Zeiss Evo40 scanning electron microscope (SEM) with an accelerating voltage varying within 5–10 kV. For elemental analysis, energy dispersive X-ray (EDX) analysis of the powder samples dispersed on an electrically conductive carbon film was performed using an accelerating voltage of 10 kV.

Crystallographic changes on the samples after calcination were determined via XRD measurements performed using a Rigaku (Japan) X-ray diffractometer equipped with a Miniflex goniometer and a monochromated high-intensity CuK $\alpha$  radiation ( $\lambda = 1.5405 \text{ \AA}$ , 30 kV, 15 mA) source. XRD data were collected by scanning the  $2\theta$  range within 10–60° using a step size of  $0.02^\circ \text{ s}^{-1}$ . Identification of the unknown phases in the powder XRD data were made by utilizing Powder Diffraction File (PDF) database maintained by the International Centre for Diffraction Data (ICDD).

Raman experiments were carried out using a LabRAM HR800 spectrometer (Horiba Jobin Yvon, Japan) equipped with a Nd:YAG laser ( $\lambda = 532.1 \text{ nm}$ , 20 mW) and an integrated confocal Olympus BX41 microscope. The system was calibrated using the reference Si Raman shift at  $520.7 \text{ cm}^{-1}$  by adjusting the zero-order position of the grating. Powder sample was evenly spread on a single crystal Si wafer and Raman spectra were recorded in the range of  $100$ – $1500 \text{ cm}^{-1}$  with a spectral resolution of  $4 \text{ cm}^{-1}$  at room temperature.

The Brunauer-Emmett-Teller (BET) SSA measurements of the synthesized catalysts were determined by nitrogen adsorption-desorption isotherms using a Micromeritics Tristar 3000 surface area and pore size analyser. Prior to SSA analysis, all samples were outgassed in vacuum for 2 h at  $150^\circ\text{C}$ .

### 2.4. Liquid phase photocatalytic activity tests for the degradation of RhB (aq)

Photocatalytic functionality of the biotemplated TiO<sub>2</sub> microspheres in liquid phase was demonstrated via *RhB* (aq) dye degradation under UVA irradiation at room temperature. *RhB* is a frequently used model pollutant for testing the photocatalytic activity of novel materials in water. *RhB* degradation experiments were performed in a photocatalytic reactor equipped with an 8W Sylvania UVA-lamp (F8W, T5, Black-light, 368 nm). A cooling fan was also installed inside the reactor for temperature regulation. Initially, a 48 mL aqueous solution of *RhB* ( $10 \text{ mg L}^{-1}$ ) was prepared in dark and 25 mg of biotemplated TiO<sub>2</sub> microspheres were ultrasonically dispersed in this solution to form a suspension. Then, the sample container was placed at a specified position inside the photocatalytic reactor, where the distance between the light source and the suspension was fixed at 13 cm. Prior to UVA light irradiation, the suspension was magnetically stirred inside the reactor under dark conditions for 30 min in order to establish an adsorption-desorption equilibrium between the photocatalyst and *RhB* (aq). Before the UVA light exposure, a 3 mL aliquot was extracted from the suspension under dark conditions and the concentration of this starting solution was designated as  $C_0$ . Then, identical amounts of samples were obtained during the UVA light irradiation after certain time intervals whose concentrations were denoted as  $C_t$ . After removing the photocatalyst from the extracted samples via centrifugation, *RhB* concentration of the extracted solutions were determined using a UV-vis spectrophotometer (Carry 300, Agilent) with the help of a calibration curve utilizing the *RhB* characteristic maximal absorption band at *ca.* 553 nm. The typical photon power density (irradiance) during the experiments was  $7.4 \text{ W m}^{-2}$  which was measured by a photo radiometer (Delta Ohm, HD2302.0, Italy) equipped with a UVA probe (DeltaOhm, LP471 UVA). The photocatalytic dye degradation efficiency ( $D_{eff}$ ) of the photocatalysts was calculated according to following equation;

$$D_{eff} (\%) = \frac{(C_0 - C_t)}{C_0} \times 100 \quad (1)$$

where,  $C_0$  is the initial *RhB* concentration and  $C_t$  is the *RhB* concentration at a given time  $t$ .

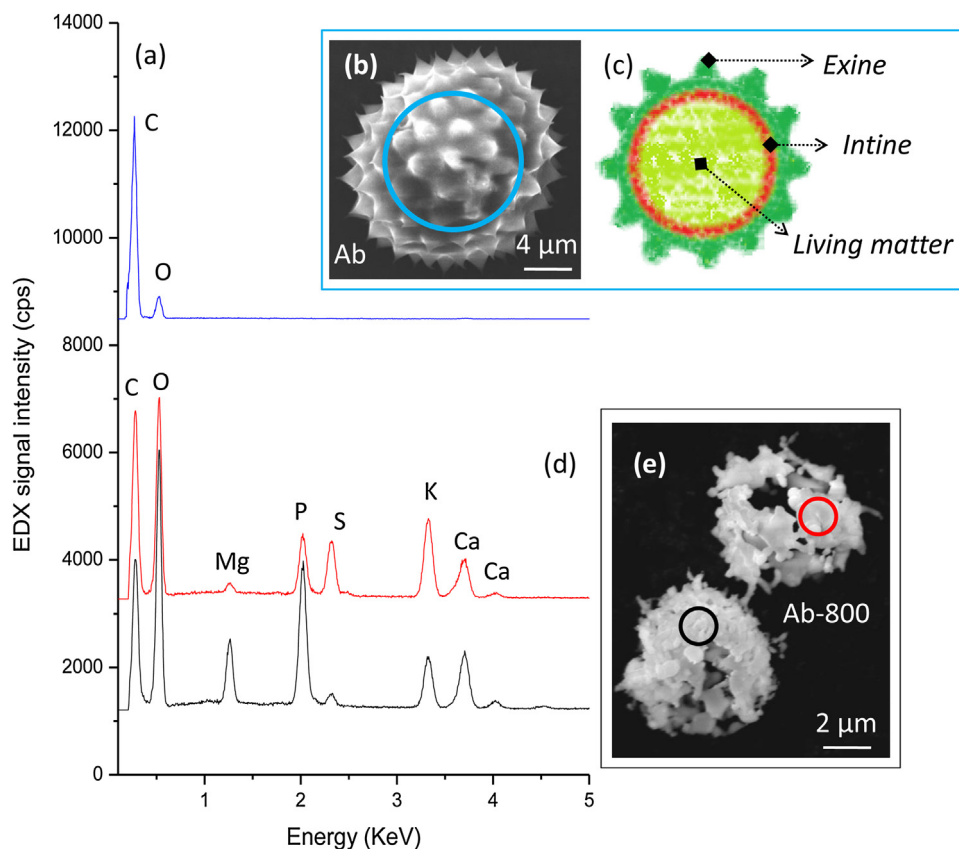


**Fig 1.** (a) EDX spectrum of the bare (uncoated) *Ab* pollen obtained from the blue-coloured circular region in (b). (b) SEM image of the uncoated *Ab* pollen. (c) Schematic describing the various bio-structural sections of the *Ab* pollen. (d) EDX spectra obtained after calcination of the uncoated *Ab* pollens at 800 °C. Red and black spectra were obtained from the circular regions with the corresponding colours presented in (e). (e) SEM image of the uncoated *Ab* pollens after calcination at 800 °C. (For interpretation of the references to colour in this figure legend, the reader is referred to the web version of this article.)

## 2.5. Gas phase photocatalytic activity tests for the removal of gaseous nitric oxide

In order to demonstrate the functional versatility of the synthesized biotemplated TiO<sub>2</sub> microspheres, in addition to the liquid phase photocatalytic tests, obtained materials were also used in photocatalytic oxidative storage of NO at the solid/gas interface. Photocatalytic removal of NO(g) over biotemplated TiO<sub>2</sub> microspheres was performed at room temperature in a custom-made continuous photocatalytic flow reactor which was designed considering the ISO 22197-1: 2007 standard [8–10,34]. This photocatalytic reaction system was composed of a gas supply unit, a flat-bed photoreactor chamber housing the sample, a UVA illumination source and a chemiluminescent NO<sub>x</sub> analyser (Horiba APNA-370) for continuous inline monitoring of the NO, NO<sub>2</sub> and total NO<sub>x</sub> concentrations [8–10]. In the gas supply unit, NO (100 ppm NO in N<sub>2</sub> balance, Linde GmbH) was mixed with O<sub>2</sub> (99.998%, Linde GmbH) and N<sub>2</sub> (99.998%, Linde GmbH) at room temperature. The total gas flow rate in the reactor was kept at ca. 1.0 SLM (standard liters per minute) via mass flow controllers (MFCs, MKS, 1479A) by adjusting the flow rate of each gas (*i.e.* N<sub>2</sub> = 0.75 SLM, O<sub>2</sub> = 0.25 SLM, and NO = 0.01 SLM). The gas mixture was also passed through a water bubbler before the reactor for humidification and the relative humidity (RH) of the gas mixture was measured via a Hanna HI 9565 humidity analyzer at the sample position in the photocatalytic reactor at room temperature. RH was detected to be typically *ca.* 70% at room temperature during the measurements. Synthesized photocatalyst powder samples (250 mg) were gently pressed on a poly-methyl methacrylate (PMMA) sample holder (2 × 20 × 20 mm<sup>3</sup>) to produce a smooth

surface. In order to activate the photocatalysts and remove the initial surface contaminants, before the gas phase photocatalytic activity measurements, samples were exposed to UVA irradiation under ambient conditions for 18 h. Then, the sample was placed into the photocatalytic reactor, where a UVA lamp (Sylvania UV-lamp, black-light, F8W, T5, 368 nm) was placed above the reactor. Next, the gas mixture was fed to the photocatalytic reactor, where the gas feed swept the surface of the powder photocatalyst sample. After establishing the adsorption-desorption equilibrium inside the photocatalytic reactor, UVA illumination source was activated to initiate the photocatalytic reaction. Control experiments carried out in the absence of a photocatalyst (*i.e.* in the empty reactor under the UVA illumination) revealed no catalytic conversion. Photocatalytic conversion efficiency for NO and photocatalytic NO<sub>2</sub> production efficiency ( $\zeta\%$ ) over TiO<sub>2</sub> microspheres were calculated as follows:

$$\zeta\% = \frac{n_{NO_x} \text{ or } n_{NO_2}}{n_{photon}} \times 100 \quad (2)$$

where,  $n_{NO_x}$  is the decrease in the total number of moles of all gaseous NO<sub>x</sub> species and  $n_{NO_2}$  is the number of moles of NO<sub>2</sub> generated in 60 min (*i.e.* over the course of a full photocatalytic NO<sub>x</sub> removal experiment). In this equation,  $n_{photon}$  corresponds to the total number of moles of incident UVA photons impinging on the catalyst surface during the 60 min time interval.  $n_{photon}$  was calculated by using the photon power density of the UVA lamp ( $I = 7.4 \text{ W m}^{-2}$ ), representative emission wavelength of the UVA lamp ( $\lambda = 368 \text{ nm}$ ), surface area of the sample holder that is exposed to the UVA irradiation ( $S = 2 \text{ cm} \times 2 \text{ cm} = 4 \text{ cm}^2$ ), duration of the

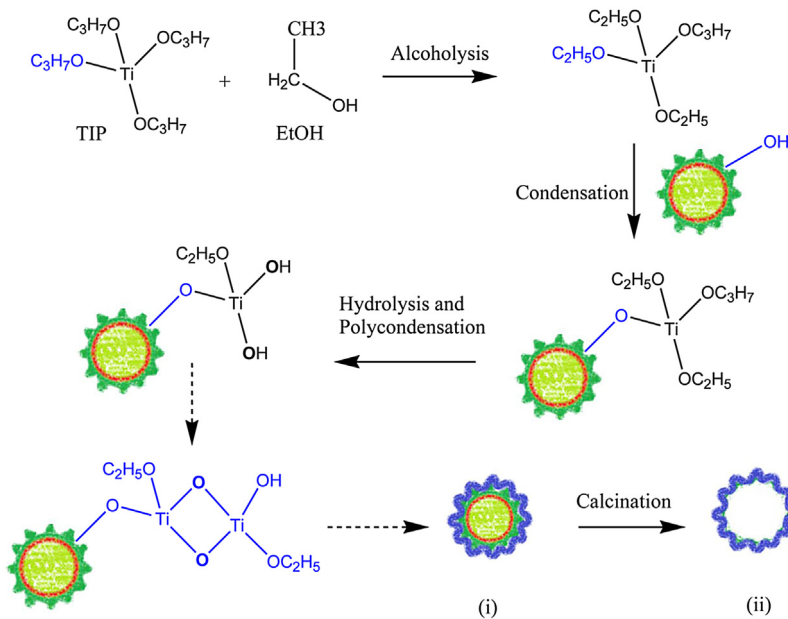


**Fig. 2.** Schematic illustration of one of the possible synthetic routes leading to the formation of biotemplated  $\text{TiO}_2$  microspheres: (i) coated  $\text{Ab}$  pollen, (ii) biotemplated  $\text{TiO}_2$  microspheres after the removal of the  $\text{Ab}$  pollen by calcination.

photocatalytic test ( $t = 3600 \text{ s}$ ), Avogadro's number ( $N_A$ ), Planck's constant ( $h$ ), and the speed of light ( $c$ ) as shown in Eq. (3) below:

$$n_{\text{photon}} = \frac{I\lambda St}{N_A h C} \quad (3)$$

### 3. Results and discussion

#### 3.1. Structure and morphology

Surface elemental composition and the morphology of the uncoated  $\text{Ab}$  pollen grains were investigated using SEM and EDX techniques (Fig. 1a and b). Macroscopic structural components of the  $\text{Ab}$  pollens were also schematically described in Fig. 1c. As can be seen in Fig. 1c,  $\text{Ab}$  pollens are composed of two nested layers covering the living matter and protecting it against the external physical and chemical adverse effects [35,36]. The robust outer surface called *exine* (Fig. 1c) is composed of a highly crosslinked organic substance that can include fatty acids, phenylpropanoids, and phenolic sporopollenins. The inner layer of the pollen (Fig. 1c) is called the *intine* and is primarily composed of cellulosic materials and polysaccharides [35,36]. In order to study the morphological and structural alterations occurring upon calcination, uncoated  $\text{Ab}$  pollen samples were investigated comparatively by SEM and EDX analysis before and after calcination (Fig. 1a–e). Fig. 1b shows that, uncoated  $\text{Ab}$  pollens have a spherical shape with an average pollen size of  $23.5 \pm 1.5 \mu\text{m}$  decorated with conical nano-spikes/thorns. After the calcination of the uncoated pollens at  $800^\circ\text{C}$ , obvious structural and morphological changes were observed signifying visible geometric deformation (Fig. 1e). According to the EDX spectra given in Fig. 1a, while uncoated microspheres have a carbonaceous outermost layer exhibiting mainly C and O signals before calcination, upon calcination at  $800^\circ\text{C}$ , pollens seem to lose their structural integrity and deform from their original shapes, revealing a variety of EDX signals corresponding to elements such C, O, Mg, P, S, K, and Ca (Figs. 1d and e). It is likely that during the calcination process, outer *exine* layer of the uncoated pollens is partially destroyed and the biological material inside the *intine* capsule, which may involve various minerals for vitality, diffuse to the

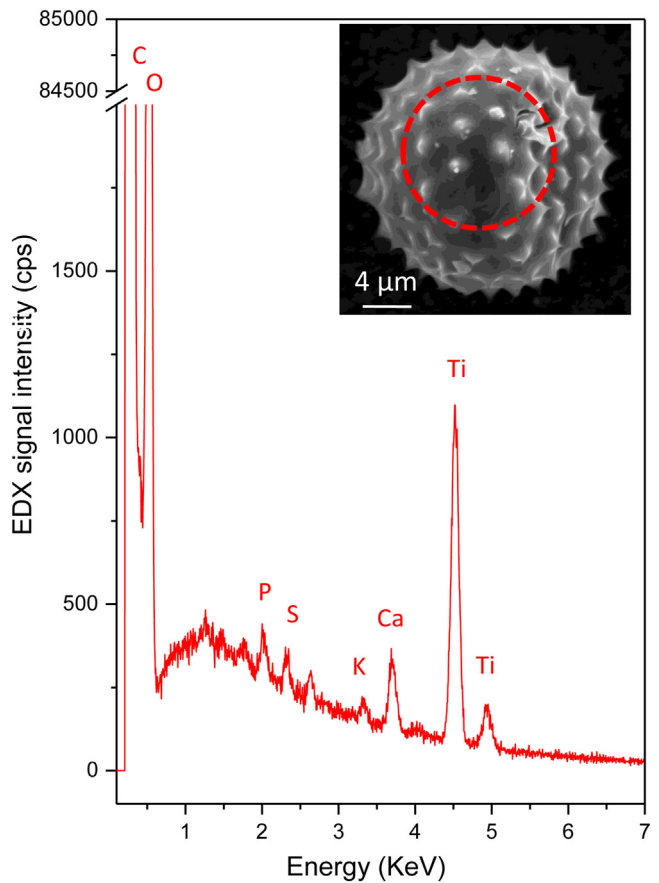


**Fig. 3.** SEM image and the corresponding EDX spectrum of the  $\text{Ab}$  biotemplate after titanium (IV) isopropoxide (TIP) deposition at  $25^\circ\text{C}$  (AbTi-25).

surface at elevated temperatures, leading to the detection of the EDX elemental signals for C, O, Mg, P, S, K, and Ca (Figs. 1d and e).

In the current work,  $\text{Ab}$  pollens were selected as a biotemplate to direct the formation of biomorphic  $\text{TiO}_2$  microspheres using the

sol-gel process. Fig. 2 provides one of the possible reaction pathways for the sol-gel synthetic route used herein. As illustrated in Fig. 2, after the alcoholysis reaction, metal alkoxide species are expected to bind to the naturally functionalized surface of the pollen template through condensation and hydrolysis reactions. Extent of the metal alkoxide deposition and the corresponding thickness of the ultimate  $\text{TiO}_2$  overlayer were controlled by the composition/concentration of the precursor solution as well as the duration of the alcoholysis reaction. After the formation of the  $\text{TiO}_2$  overlayer, calcination process leads to the formation of a biomorphic  $\text{TiO}_2$  surface preserving most of the original shape, size, and morphology of the *Ab* biotemplate.

Fig. 3 shows the SEM image and the corresponding EDX spectrum of the  $\text{TiO}_x$  deposited *Ab* pollens after hydrolysis and polycondensation reactions at room temperature (*i.e.* before calcination). SEM image reveals the formation of a homogeneous/continuous  $\text{TiO}_x$  overlayer preserving the characteristic microstructure of the nascent pollen surface. This is also evident by the EDX spectrum in Fig. 3, indicating a strong Ti signal overwhelming that of the other pre-existing elements on the surface such as Ca, S, K, and P.

Calcination was employed in order to convert amorphous  $\text{TiO}_x$  coating on the *Ab* pollens into crystalline  $\text{TiO}_2$  overlayers (Fig. 4). Low-magnification SEM image (Fig. 4a) shows that  $\text{TiO}_2$  microspheres are relatively well-dispersed rather than severely aggregated. While the calcination process induces the crystallization of the  $\text{TiO}_x$  overlayer to  $\text{TiO}_2$ , it also leads to morphological modifications at the nanometer scale resulting in the formation of a spongy/porous and a corrugated network on the surface (Fig. 4b–d and f). Comparison of the bare *Ab* (Fig. 1b) or coated *Ab* pollens before calcination (*AbTi-25*, Fig. 3), with the ones obtained after calcination (*e.g.* 600 °C and 800 °C) suggests deformation of the sharp conical spikes (Fig. 4b–d and f), in addition to the shrinking of the pollens to a smaller average diameter of *ca.* 13  $\mu\text{m}$ .

After calcination (Fig. 4e), P, K, and Ca signals originating from the biotemplate becomes discernible on the *AbTi-600* and *AbTi-800* surfaces. It can be seen in Figs. 4b and 4e that an aperture with an approximate diameter of 2.5  $\mu\text{m}$  exists in the *Ab* pollen structure, from which the pollen tube extends at germination to fertilize the ovum. Thus, it is feasible that during the calcination process, the interior part of the pollen (*i.e.* *intine* and other biological living matter depicted in Fig. 1c) diffuses outbound through this aperture and spilled over on the  $\text{TiO}_2$  surface at elevated temperatures.

Fig. 5a and b illustrate the phase changes occurring on the *AbTi* materials as a function of calcination temperature via XRD and Raman spectroscopy, respectively. It is apparent that the diffraction signals in Fig. 5a intensify and sharpen with increasing calcination temperatures suggesting ordering and crystallization of the  $\text{TiO}_2$  overlayer on the *AbTi* surface. XRD patterns of the *AbTi* microspheres reveal predominantly anatase phase at calcination temperatures  $\leq 600$  °C; while two different ordered  $\text{TiO}_2$  phases namely, anatase (ICDD No. 00-021-1272) and rutile (ICDD No. 00-021-1276) are visible for the calcination temperatures above 600 °C (Fig. 5a). Also, Fig. 6 depicts relative mass fraction of anatase and rutile phases for various samples calculated using the XRD data via Spurr and Myers approach [37]. It is clear that the anatase to rutile phase transition on the *Ab* surface starts to occur predominantly at  $T \geq 800$  °C. Rutile mass fraction increases drastically for  $T \geq 800$  °C, while for the *AbTi-900* sample, anatase and rutile phases reveal almost equal mass fractions.

Average crystallite sizes of the anatase and rutile phases were also calculated using the anatase (101) and rutile (110) diffraction signals via Scherrer equation [38,39] (Fig. 6). These results suggest that anatase and rutile domains have similar average crystallite sizes (*ca.* 20–30 nm) for *AbTi-700* and *AbTi-800* samples while they drastically diverge from each other for the *AbTi-900* sample, where

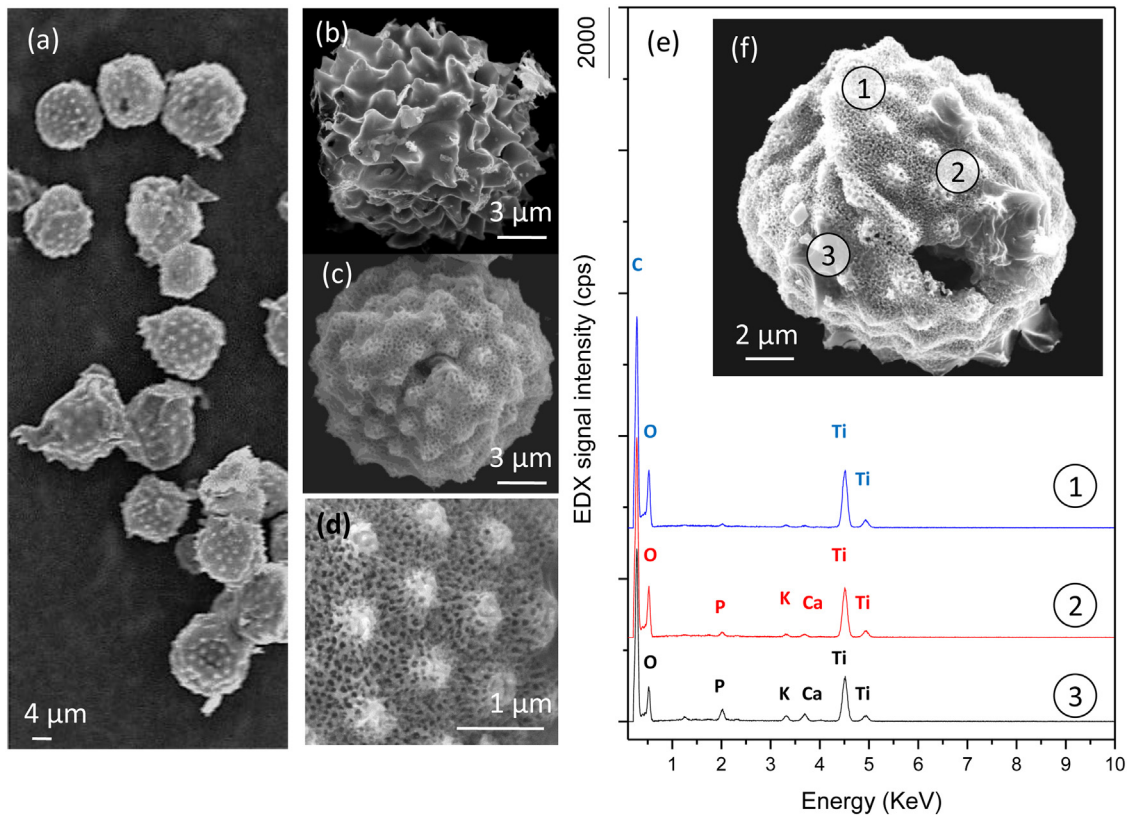
rutile crystallite size surpasses that of the anatase (*ca.* 47 nm for anatase and *ca.* 134 nm for rutile). Fig. 6 indicates that increasing calcination temperatures results in a monotonic increase in the crystallite sizes of anatase and rutile domains due to sintering.

Raman spectroscopic measurements were also performed in order to confirm the structural properties of the biotemplated  $\text{TiO}_2$  microspheres. Fig. 5b displays the Raman spectra of the samples prepared by calcination of the coated *AbTi* samples at different temperatures. Characteristic anatase Raman scattering features at 147  $\text{cm}^{-1}$  (Eg), 397  $\text{cm}^{-1}$  (B1 g), 515  $\text{cm}^{-1}$  (A1 g), and 641  $\text{cm}^{-1}$  (Eg) are observed for all samples except the *AbTi-400* sample. For the *AbTi-900* sample, additional Raman peaks at 445  $\text{cm}^{-1}$  (Eg) and 612  $\text{cm}^{-1}$  (A1 g) are visible which can be attributed to the rutile phase. In good accordance with the current XRD measurements (Fig. 5a), Raman data in Fig. 5b also indicate that the rutile content of the samples increases with increasing calcination temperatures. In addition to these signals, some of the Raman spectra in Fig. 5b also includes an additional feature at 484  $\text{cm}^{-1}$  (labelled “with the symbol “♦” in Fig. 5b) which can tentatively be attributed to complex temporal species generated during the calcination of the biopolymer matrix of the underlying Ambrosia template [7].

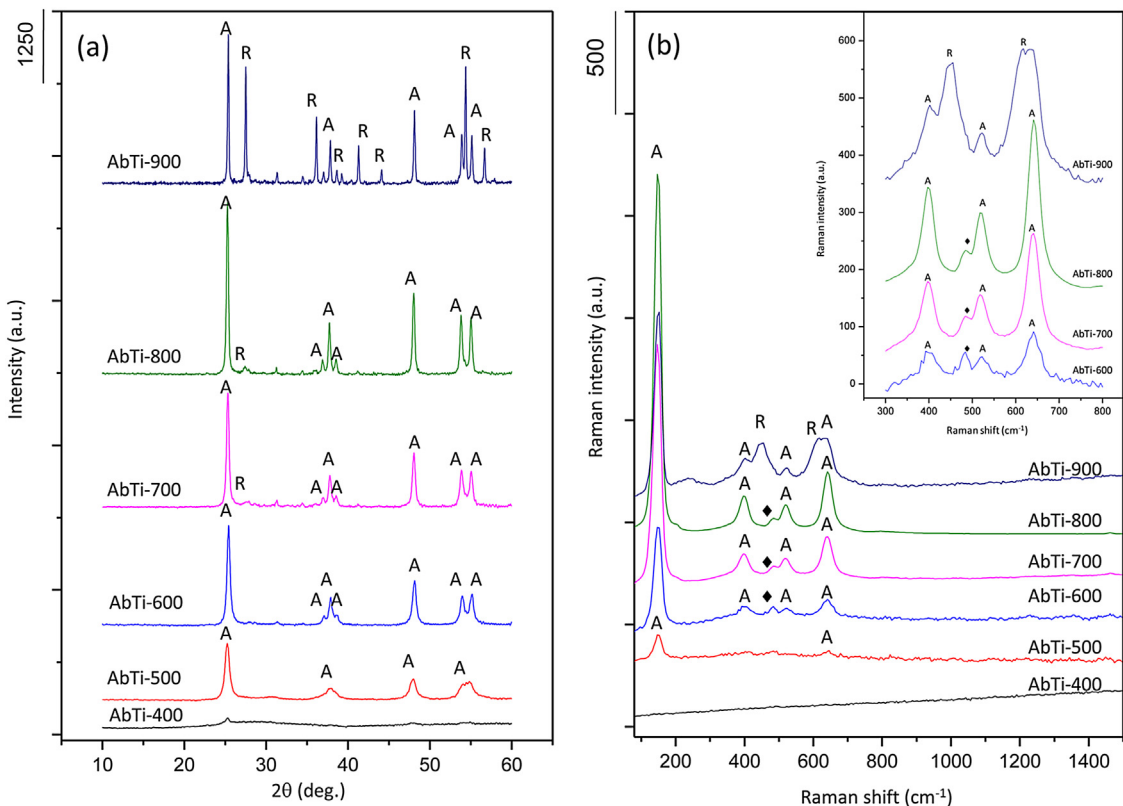
### 3.2. Photocatalytic activity of the biotemplated $\text{TiO}_2$ microspheres

Fig. 7a presents the photocatalytic *RhB* (aq) degradation studies performed under UVA irradiation at room temperature by using biotemplated  $\text{TiO}_2$  microspheres calcined at various temperatures. Fig. 7b shows a typical series of time-dependent UV-vis absorption spectra of the *RhB*(q) containing the *AbTi-800* sample obtained during the UVA irradiation. It is apparent that the characteristic *RhB* absorption band at 553 nm gradually decreases while the photocatalytic dye degradation reaction proceeds. After 120 min UVA light exposure, color originating from *RhB* dye is virtually disappears evident by the vanishing absorption signal at 553 nm. Note that the photocatalytic *RhB* (aq) degradation performance of the *AbTi-400* sample is not reported in Fig. 7. This is due to the fact that such low calcination temperatures do not allow the complete removal of the biotemplate which in turn, leads to the formation of grains with low material density that can float on the top of the *RhB* (aq) solution preventing their homogenous mixing and uniform irradiation.

As a standard control experiment, measured decrease in *RhB* concentration of the *RhB* (aq) solution under UVA irradiation in the absence of a catalyst was also monitored in order to investigate the non-catalytic self photodegradation of the *RhB* dye (Fig. 7a). As can be seen in Fig. 7a, within 500–800 °C, increasing calcination temperature leads to a monotonic enhancement in the photocatalytic *RhB* (aq) degradation. However, calcination at higher temperatures such as 900 °C results in an attenuation of the photocatalytic *RhB* (aq) decomposition performance. Based on the structural characterization data provided in Fig. 6 and the liquid phase photocatalytic activity data given in Fig. 7, it can be realised that the optimum photocatalyst sample for *RhB* (aq) degradation (*i.e.* *AbTi-800*) is comprised of both anatase and rutile domains with a specific surface area of *ca.* 7–8  $\text{m}^2/\text{g}$ . It is also apparent that the monotonic increase in the photocatalytic *RhB* (aq) decomposition performance within 500–800 °C is concomitant to the increase in the crystallinity as well as the average size of the anatase domains, where the latter converges to *ca.* 30 nm for the *AbTi-800* sample. Fig. 6 also suggests that the *AbTi-800* sample is comprised of 94.9% anatase and 5.1% rutile by mass. On the other hand, at elevated calcination temperatures such as 900 °C, relative rutile mass fraction increases to values above the optimal value, leading to attenuation in the photocatalytic performance (Figs. 6 and 7). It is apparent that the optimum bio-templated photocatalyst studied in the current work for the *RhB* (aq) degradation processes possesses co-existing anatase and rutile domains functioning in a synergistic manner with



**Fig. 4.** SEM images of the biotemplated TiO<sub>2</sub> microspheres calcined for 2.5 h in air at (a) 800 °C (low magnification image, AbTi-800) (b) 600 °C (AbTi-600), and (c, d, and (e) 800 °C (AbTi-800). Image (d) also emphasizes the SEM image showing the detailed morphology of the AbTi-800 pollen surface exhibiting a porous and a corrugated TiO<sub>2</sub> overlayer structure. (e) EDX spectra obtained from the circled regions labelled as 1, 2, 3 in (f).



**Fig. 5.** (a) XRD patterns and (b) the Raman spectra of the biotemplated TiO<sub>2</sub> microspheres calcined at 400, 500, 600, 700, 800, and 900 °C for 2.5 h in air after coating. "A" and "R" letters correspond to anatase and rutile phases; respectively (see text for details).

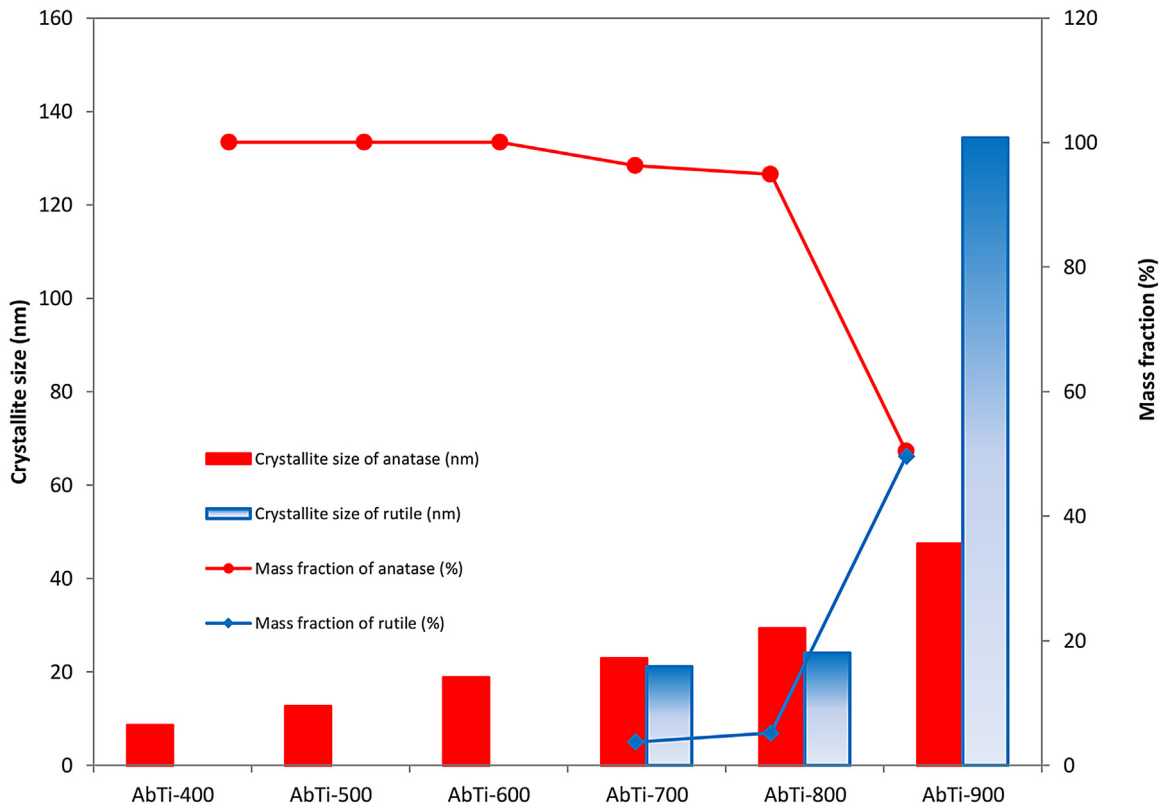


**Fig. 6.** Variation of the anatase and rutile average crystallite sizes and mass fractions on the coated *AbTi* samples as a function of calcination temperature.

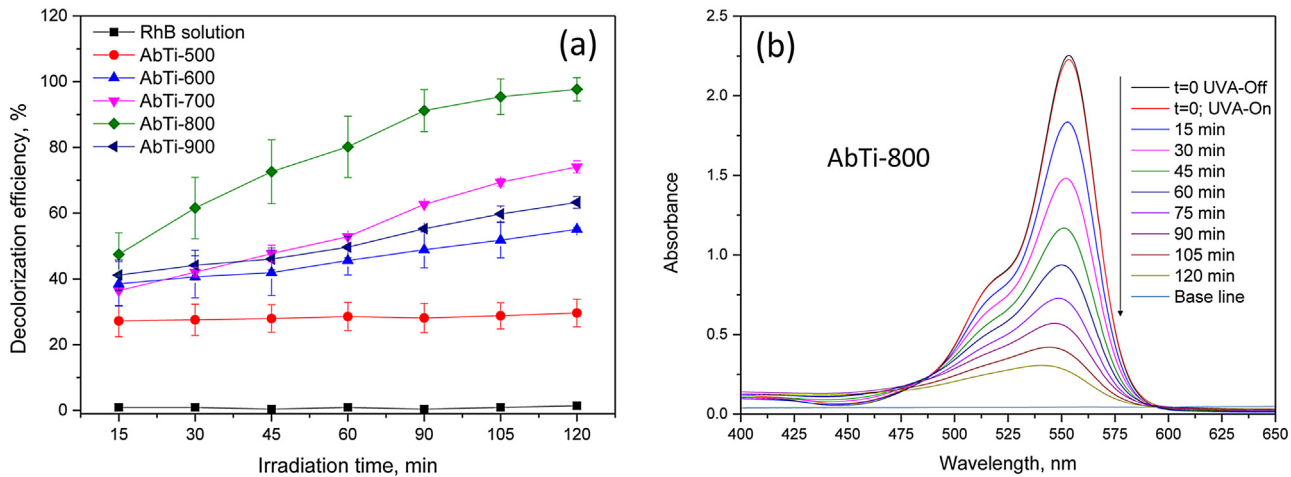


**Fig. 7.** (a) Photocatalytic *RhB* (aq) degradation performance of biotemplated  $\text{TiO}_2$  microspheres under UVA illumination at room temperature. Measurement labelled as the “*RhB* Solution” was performed in the absence of a photocatalyst under UVA irradiation. (b) Time-dependent UV-vis absorption spectra of the *AbTi*-800 sample during the photocatalytic *RhB* (aq) degradation process.

particular crystallite sizes and a unique mass fraction. This observation is in perfect agreement with former photocatalytic studies on other  $\text{TiO}_2$ -based systems in the literature [40–42]. It should be noted that the photocatalytic activity of *AbTi* systems are typically lower than that of a conventional benchmark catalyst such as Degussa P25 revealing% photonic efficiencies of 0.45 and 0.11 for  $\text{NO}_2(\text{g})$  production and  $\text{NOx}$  storage; respectively. This can be attributed to the higher SSA of P25 (*ca.* 50  $\text{m}^2/\text{g}$ ).

After having demonstrated the photocatalytic water purification capabilities of the *Ab*-tempalited  $\text{TiO}_2$  microspheres under UVA irradiation, we performed further studies in order to establish the photocatalytic activity of this new family of materials in photocat-

alytic air purification applications. Along these lines, photocatalytic  $\text{NO}(\text{g})$  oxidation and storage experiments were carried out using a custom-made photocatalytic flow reactor under UVA irradiation [8–10]. Fig. 8 presents results of these gas phase photocatalytic activity tests. The resulting typical time-dependent concentration profiles for the photocatalytic  $\text{NO}$  oxidative storage experiment is also shown in the inset of Fig. 8. In the histograms of Fig. 8, per cent photonic efficiency values for total  $\text{NOx}$  removal (blue bars) and  $\text{NO}_2$  production (red bars) are shown. It is worth mentioning that an ideal photocatalyst for gas phase De $\text{NOx}$  applications should exhibit a high  $\text{NOx}(\text{g})$  storage/removal efficiency as well as low  $\text{NO}_2(\text{g})$  generation/release characteristics. Photocatalytic oxidative

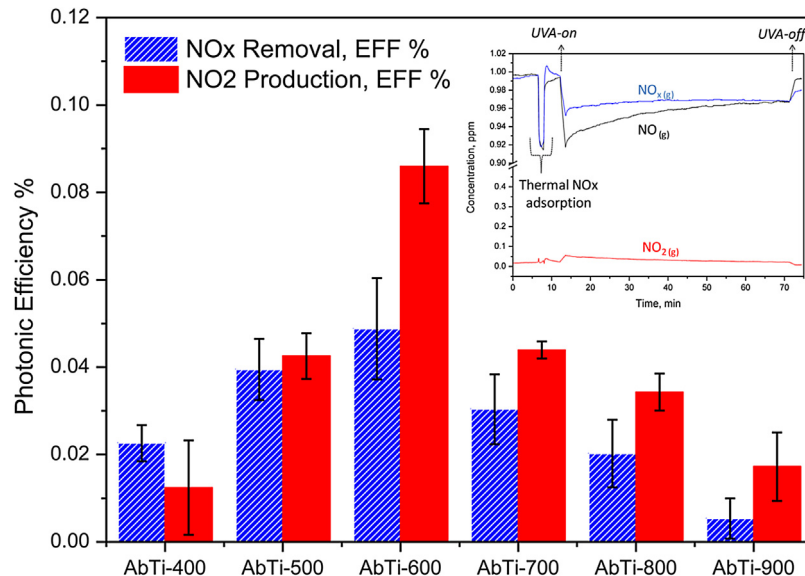


**Fig. 8.** Photocatalytic NO(g) oxidation and storage performance results obtained via UVA irradiation at room temperature for biotemplated TiO<sub>2</sub> microspheres initially calcined at various temperatures (inset shows the typical time-dependent concentration profiles for total NO<sub>x</sub>(g), NO(g), and NO<sub>2</sub>(g) over AbTi-600. (For interpretation of the references to colour in text, the reader is referred to the web version of this article.)

storage of NO(g) includes oxidation steps [11,34,43,44] involving the formation of NO<sub>2</sub>(g), where the eventual storage of NO<sub>x</sub> species on the catalyst surface may occur in the form of chemisorbed NO, NO<sub>2</sub>/NO<sub>2</sub><sup>-</sup>, N<sub>2</sub>O, and NO<sub>3</sub><sup>-</sup>. Thus, maximizing the oxidative NO<sub>x</sub> storage at the solid state, while simultaneously minimizing the gas phase release of toxic NO<sub>2</sub>(g) requires optimization of the chemical, electronic and surface structure of the photocatalysts.

Along these lines, photocatalytic DeNO<sub>x</sub> performance of the synthesized *AbTi* photocatalysts were investigated as a function of the calcination temperature used in the synthetic protocol, in an attempt to monitor the structure-functionality relationships. Photocatalytic activity data presented in Fig. 8 can be analysed in the light of these arguments (Figs. 1–6). It is apparent that unlike the liquid phase *RhB* (aq) degradation results given in Fig. 7, suggesting *AbTi*-800 as the optimum catalyst in the liquid phase, Fig. 8 shows that *AbTi*-800 has limited photocatalytic NO<sub>x</sub> abatement capability in gas phase. This observation may suggest relatively different reaction mechanisms and involvement of dissimilar active sites for the photocatalytic liquid phase water purification processes as compared to the gas phase photocatalytic DeNO<sub>x</sub> processes occurring on the same catalyst surface.

The highest total photocatalytic gas phase activity can be assigned to the *AbTi*-600 catalyst given in Fig. 8 due to the fact that this catalyst reveals maximum NO<sub>x</sub> removal efficiency and maximum photocatalytic oxidation of NO(g) to NO<sub>2</sub>(g). On the other hand, *AbTi*-600 should not be identified as the photocatalyst of choice due to its high NO<sub>2</sub>(g) release to the atmosphere. Comparison of the *AbTi*-600 catalyst with *AbTi*-500 reveals that the *AbTi*-500 has a comparable NO<sub>x</sub> storage efficiency to that of the *AbTi*-600 catalyst, while exhibiting much lower NO<sub>2</sub>(g) release. Hence, *AbTi*-500 can be considered as the preferable catalyst in the series for gas phase photocatalytic DeNO<sub>x</sub> applications. It is likely that the gas phase photocatalytic oxidation of NO(g) requires the presence of ordered anatase domains, while prevention of the NO<sub>2</sub>(g) slip to the atmosphere requires a porous/high surface area catalyst that can optimize capture/adsorption/solid state storage of the generated NO<sub>2</sub>(g). This is consistent with the observation that the *AbTi*-400 catalyst obtained after a low-temperature calcination step has limited NO<sub>x</sub> removal efficiency as well as low NO<sub>2</sub>(g) production, due to the lack of ordered anatase domains and

presence of small anatase particles and disordered (amorphous) domains. In other words, the main reason for the poor performance of *AbTi*-400 seems to be its limited photocatalytic oxidation capability rather than its lack of surface area for NO<sub>x</sub> storage. In contrast, for the catalysts calcined at T ≥ 700 °C, the main catalytic disadvantage could be shrinking of the pollens at high temperatures (i.e. decrease in the available surface sites for adsorption and storage of oxidized NO<sub>x</sub> species) and decrease in the number of exposed active sites, which in turn hinder the storage of photocatalytically produced NO<sub>2</sub> species, resulting in detrimental NO<sub>2</sub> release to the atmosphere. Comparison of the liquid phase photocatalytic activity of *AbTi* systems with that of a benchmark catalyst (i.e. Degussa P25) reveals that the latter system has a higher photocatalytic activity, where 100% decolorization efficiency can be reached after ca. 70 min. This observation can be associated with the higher surface area of the latter system.

#### 4. Conclusions

A novel biotemplate-based photocatalytic material platform was synthesized by utilizing *Ambrosia trifida* (*Ab*, Giant ragweed) pollen as the initial biological support surface. Structural characterization of the synthesized biotemplated TiO<sub>2</sub> microspheres was performed using SEM-EDX, Raman spectroscopy, and XRD techniques. Photocatalytic functionality of the synthesized materials was demonstrated both in gas phase (via photocatalytic oxidative NO<sub>x</sub> storage) as well as in liquid phase (via photocatalytic Rhodamine B (aq) degradation) as a function of the calcination temperature used in the synthetic protocol. Optimum catalyst for *RhB*(aq) photocatalytic degradation in the liquid phase was found to be *AbTi*-800, while the optimum catalyst for gas phase photocatalytic oxidative NO<sub>x</sub> storage was *AbTi*-500; emphasizing different structural/functional requirements for different catalytic reactions occurring on the same catalytic surface. The synthetic approach presented herein offers new opportunities for obtaining advanced functional materials which can have potential prospective applications in micro reactor systems, adsorbents, drug delivery systems, catalytic processes, and sensor technologies.

## Acknowledgments

EO acknowledges financial support from “The Science Academy” (Turkey) through “Young Scientists Award Program (BAGEP)”. Authors also acknowledge the scientific collaboration with TARLA project founded by the Ministry of Development of Turkey under grant no DPT2006K-120470.

## References

- [1] F. Dong, Y. Sun, M. Fu, W. Ho, S.C. Lee, Z. Wu, Novel in situ N-doped ( $\text{BiO}$ )<sub>2</sub> CO<sub>3</sub> hierarchical microspheres self-assembled by nanosheets as efficient and durable visible light driven photocatalyst, *Langmuir* 28 (2012) 766–773.
- [2] F. Dong, S.C. Lee, Z. Wu, Y. Huang, M. Fu, W. Ho, S. Zou, B. Wang, Rose-like monodisperse bismuth subcarbonate hierarchical hollow microspheres: one-pot template-free fabrication and excellent visible light photocatalytic activity and photochemical stability for NO removal in indoor air, *J. Hazard. Mater.* 195 (2011) 346–354.
- [3] S. Shen, M. Burton, B. Jobson, L. Haselbach, Pervious concrete with titanium dioxide as a photocatalyst compound for a greener urban road environment, *Constr. Build. Mater.* 35 (2012) 874–883.
- [4] S.W. Verbruggen, TiO<sub>2</sub> photocatalysis for the degradation of pollutants in gas phase: from morphological design to plasmonic enhancement, *J. Photochem. Photobiol. C Photochem. Rev.* 24 (2015) 64–82.
- [5] X. Shao, W. Lu, R. Zhang, F. Pan, C. Tio, Enhanced photocatalytic activity of TiO<sub>2</sub> –C hybrid aerogels for methylene blue degradation, *Sci. Rep.* 3 (2013) 1–9.
- [6] D.A. Erdogan, M. Sevim, E. Kisa, D.B. Emiroglu, M. Karatok, E.I. Vovk, M. Bjerring, Ü. Akbey, Ö. Metin, E. Ozensoy, Photocatalytic activity of mesoporous graphitic carbon nitride (mpg-C<sub>3</sub>N<sub>4</sub>) towards organic chromophores under UV and VIS light illumination, *Top. Catal.* 59 (2016) 1305–1318.
- [7] D.A. Erdogan, T. Solouki, E. Ozensoy, A versatile bio-inspired material platform for catalytic applications: micron-sized buckyball-shaped TiO<sub>2</sub> structures, *RSC Adv.* 5 (2015) 47174–47182.
- [8] D.A. Erdogan, M. Polat, R. Garifullin, M.O. Guler, E. Ozensoy, Thermal evolution of structure and photocatalytic activity in polymer microsphere templated TiO<sub>2</sub> microbowls, *Appl. Surf. Sci.* 308 (2014) 50–57.
- [9] A.M. Soylu, M. Polat, D.A. Erdogan, Z. Say, C. Yildirim, Ö. Birer, E. Ozensoy, TiO<sub>2</sub>-Al<sub>2</sub>O<sub>3</sub> binary mixed oxide surfaces for photocatalytic NO<sub>x</sub> abatement, *Appl. Surf. Sci.* 318 (2014) 142–149.
- [10] M. Polat, A.M. Soylu, D.A. Erdogan, H. Erguvan, E.I. Vovk, E. Ozensoy, Influence of the sol-gel preparation method on the photocatalytic NO oxidation performance of TiO<sub>2</sub>/Al<sub>2</sub>O<sub>3</sub> binary oxides, *Catal. Today* 241 (2015) 25–32.
- [11] W. Lu, A.D. Olaitan, M.R. Brantley, B. Zekavat, D.A. Erdogan, E. Ozensoy, T. Solouki, Photocatalytic conversion of nitric oxide on titanium dioxide: cryotrapping of reaction products for online monitoring by mass spectrometry, *J. Phys. Chem. C* 120 (2016) 8056–8067.
- [12] G. Shi, B. Zhang, X. Xu, Y. Fu, Graphene oxide coated coordination polymer nanobelt composite material: a new type of visible light active and highly efficient photocatalyst for, *Dalton Trans.* 44 (2015) 11155–11164.
- [13] Q. Zhang, Y. Huang, L. Xu, J. Cao, W. Ho, S.C. Lee, Visible-light-active plasmonic Ag-SrTiO<sub>3</sub> nanocomposites for the degradation of NO in air with high selectivity, *ACS Appl. Mater. Interfaces* 8 (2016) 4165–4174.
- [14] Y. Zhu, P. Wu, S. Yang, Y. Lu, W. Li, RSC advances synergistic effect of functionalized carbon nanotubes on ZnCr<sub>x</sub>–mixed metal oxides for enhanced solar light-driven photocatalytic performance, *RSC Adv.* 6 (2016) 37689–37700.
- [15] L. Pan, T. Muhammad, L. Ma, Z. Huang, S. Wang, L. Wang, J. Zou, X. Zhang, MOF-derived C-doped ZnO prepared via a two-step calcination for efficient photocatalysis, *Appl. Catal. B Environ.* 189 (2016) 181–191.
- [16] G. Meenakshi, A. Sivasamy, G.A.S. Josephine, S. Kavithaa, Preparation, characterization and enhanced photocatalytic activities of zinc oxide nano rods/silicon carbide composite under UV and visible light irradiations, *J. Mol. Catal. A Chem.* 411 (2016) 167–178.
- [17] G. Jiang, X. Zheng, Y. Wang, T. Li, X. Sun, Photo-degradation of methylene blue by multi-walled carbon nanotubes/TiO<sub>2</sub> composites, *Powder Technol.* 207 (2011) 465–469.
- [18] H. Guo, J. Chen, W. Weng, S. Li, Hydrothermal synthesis of C-doped Zn<sub>3</sub>(OH)<sub>2</sub>V<sub>2</sub>O<sub>7</sub> nanorods and their photocatalytic properties under visible light illumination, *Appl. Surf. Sci.* 257 (2011) 3920–3923.
- [19] A. Fujishima, K. Honda, Electrochemical photolysis of water at a semiconductor electrode, *Nature* 238 (1972) 37–38.
- [20] K. Nakata, A. Fujishima, TiO<sub>2</sub> photocatalysis: design and applications, *J. Photochem. Photobiol. C Photochem. Rev.* 13 (2012) 169–189.
- [21] R. Daghrir, P. Drogui, D. Robert, Modified TiO<sub>2</sub> for environmental photocatalytic applications: a review, *Ind. Eng. Chem. Res.* 52 (2013) 3581–3599.
- [22] J. Tian, Z. Zhao, A. Kumar, R.I. Boughton, H. Liu, Recent progress in design, synthesis, and applications of one-dimensional TiO<sub>2</sub> nanostructured surface heterostructures: a review, *Chem. Soc. Rev.* 43 (2014) 6920–6937.
- [23] J. Shi, S. Chen, Z. Ye, S. Wang, P. Wu, Favorable recycling photocatalyst TiO<sub>2</sub>/CFA: effects of loading percent of TiO<sub>2</sub> on the structural property and photocatalytic activity, *Appl. Surf. Sci.* 257 (2010) 1068–1074.
- [24] A. Simpraditpan, T. Wirunmongkol, S. Pavasupree, W. Pecharapa, Effect of calcination temperature on structural and photocatalyst properties of nanofibers prepared from low-cost natural ilmenite mineral by simple hydrothermal method, *Mater. Res. Bull.* 48 (2013) 3211–3217.
- [25] Y. Obukuro, S. Matsushima, K. Obata, T. Suzuki, M. Arai, Effects of La doping on structural, optical, electronic properties of Sr<sub>2</sub>Bi<sub>2</sub>O<sub>5</sub> photocatalyst, *J. Alloys Compd.* 658 (2016) 139–146.
- [26] Y.J. Kim, X. Xing, D.-Y. Choi, C.-H. Hwang, C. Choi, G. Kim, S. Jin, K.-J. Hwang, J.-Y. Park, Study of the photocatalytic properties of bio-mimicked hollow SnO<sub>2</sub> microstructures synthesized with *Ceiba pentandra* (L.) Gaertn. (kapok) as a natural template, *New J. Chem.* 39 (2015) 7754–7758.
- [27] B. Li, J. Zhao, J. Liu, X. Shen, S. Mo, H. Tong, Bio-templated synthesis of hierarchically ordered macro-mesoporous anatase titanium dioxide flakes with high photocatalytic activity, *RSC Adv.* 5 (2015) 15572–15578.
- [28] G. Xiao, X. Huang, X. Liao, B. Shi, One-pot facile synthesis of cerium-doped TiO<sub>2</sub> mesoporous nano fibers using collagen fiber as the biotemplate and its application in visible light photocatalysis, *J. Phys. Chem. C* (2013) 9739–9746.
- [29] A. Ahamed Fazil, J. Udaya Bhanu, A. Amutha, S. Joicy, N. Ponpandian, S. Amirthapandian, B.K. Panigrahi, P. Thangadurai, A facile bio-replicated synthesis of SnO<sub>2</sub> motifs with porous surface by using pollen grains of *Peltoperphorum pterocarpum* as a template, *Microporous Mesoporous Mater.* 212 (2015) 91–99.
- [30] F. Cao, D.-X. Li, Morphology-controlled synthesis of SiO<sub>2</sub> hollow microspheres using pollen grain as a biotemplate, *Biomed. Mater.* 4 (2009) 25009.
- [31] Z. He, W. Que, Y. He, Synthesis and characterization of bioinspired hierarchical mesoporous TiO<sub>2</sub> photocatalysts, *Mater. Lett.* 94 (2013) 136–139.
- [32] J. Qian, Z. Chen, C. Liu, X. Lu, F. Wang, M. Wang, Improved visible-light-driven photocatalytic activity of CeO<sub>2</sub> microspheres obtained by using lotus flower pollen as biotemplate, *Mater. Sci. Semicond. Process.* 25 (2014) 27–33.
- [33] W. Zhu, H. Huang, W. Zhang, X. Tao, Y. Gan, Y. Xia, H. Yang, X. Guo, Synthesis of MnO/C composites derived from pollen template for advanced lithium-ion batteries, *Electrochim. Acta* 152 (2015) 286–293.
- [34] A. Mills, S. Elouali, The nitric oxide ISO photocatalytic reactor system: measurement of NO<sub>x</sub> removal activity and capacity, *J. Photochem. Photobiol. A Chem.* 305 (2015) 29–36.
- [35] B.J. Howlett, R.B. Knox, J. Heslop-Harrison, Pollen-wall proteins: release of the allergen antigen e from intine and exine sites in pollen grains of ragweed and cosmos, *J. Cell Sci.* 13 (1973) 603–619.
- [36] S.L. Atkin, S. Barrier, Z. Cui, P.D.I. Fletcher, G. Mackenzie, V. Panel, V. Sol, X. Zhang, UV and visible light screening by individual sporopollenin exines derived from *Lycopodium clavatum* (club moss) and *Ambrosia trifida* (giant ragweed), *J. Photochem. Photobiol. B Biol.* 102 (2011) 209–217.
- [37] R.A. Spurr, H. Myers, Quantitative analysis of anatase-rutile mixtures with an X-ray diffractometer, *Anal. Chem.* 29 (1957) 760–762.
- [38] P. Scherrer, Bestimmung der Größe und der inneren Struktur von Kolloidteilchen mittels Röntgenstrahlen, *Göttinger Nachrichten Gesell 2* (1918) 98–100.
- [39] M. Černá, M. Veselý, P. Dzik, C. Guillard, E. Puzenat, M. Lepičová, Fabrication, characterization and photocatalytic activity of TiO<sub>2</sub> layers prepared by inkjet printing of stabilized nanocrystalline suspensions, *Appl. Catal. B Environ.* 138 (2013) 84–94.
- [40] Z.G. Xiong, H. Wu, L.H. Zhang, Y. Gu, X.S. Zhao, Synthesis of TiO<sub>2</sub> with controllable ratio of anatase to rutile, *J. Mater. Chem. A* 2 (2014) 9291–9297.
- [41] S. Li, J. Chen, F. Zheng, Y. Li, F. Huang, Synthesis of the double-shell anatase-rutile TiO<sub>2</sub> hollow spheres with enhanced photocatalytic activity, *Nanoscale* 5 (2013) 12150–12155.
- [42] C.C. Pei, W.W.F. Leung, Enhanced photocatalytic activity of electrospun TiO<sub>2</sub>/ZnO nanofibers with optimal anatase/rutile ratio, *Catal. Commun.* 37 (2013) 100–104.
- [43] M.M. Ballari, Q.L. Yu, H.J.H. Brouwers, Experimental study of the NO and NO<sub>2</sub> degradation by photocatalytically active concrete, *Catal. Today* 161 (2011) 175–180.
- [44] X. Ding, X. Song, P. Li, Z. Ai, L. Zhang, Efficient visible light driven photocatalytic removal of NO with aerosol flow synthesized B, N-codoped TiO<sub>2</sub> hollow spheres, *J. Hazard. Mater.* 190 (2011) 604–612.